THE ASTROPHYSICAL JOURNAL, 408:514–529, 1993 May 10

SPATIAL SPECTRAL INDEX VARIATIONS IN GALACTIC SHELL SUPERNOVA REMNANTS G39.2−0.3 AND G41.1−0.3

MARTHA C. ANDERSON AND LAWRENCE RUDNICK
Astronomy Department, University of Minnesota, 116 Church Street SE, Minneapolis, MN 55455
Received 1992 August 31; accepted 1992 November 5

ABSTRACT

Spatial variations are observed in the synchrotron spectra of Galactic shell supernova remnants G39.2−0.3 and G41.1−0.3 (3C 396 and 3C 397). Spectral indices in these remnants, as measured between $\lambda 6$ and 20 cm, vary on the order of $\Delta\alpha \sim 0.2$. In neither remnant do the spectral variations correlate well with features in total radio intensity. Explanations for these variations are sought in terms of various models of astrophysical particle acceleration. In comparing G39.2−0.3 and G41.1−0.3 with seven other shell remnants exhibiting spatially varying spectral indices, we find that in the older of these remnants, brighter regions tend to be flatter. In the younger remnants, the highest emissivity regions are generally the steepest, but with notable exceptions. We suggest that interactions between the expanding remnant and inhomogeneities in the surrounding medium may be a very important factor in determining the spatial distribution of spectral indices in shell supernova remnants.

Subject headings: acceleration of particles — ISM: individual (G39.2−0.3, G41.1−0.3) — radiation mechanisms: miscellaneous — radio continuum: interstellar — supernova remnants

1. INTRODUCTION

Galactic supernova remnants (SNRs) are generally considered to be the primary acceleration sites for cosmic rays with energies up to 10^{14} eV nucleon^{-1}. It is thought that these particles are accelerated via first- or second-order Fermi processes in the shocks and/or turbulence set up by the supersonic expansion of the supernova ejecta. Many details of the SNR cosmic-ray acceleration process are not well established, observationally. It is not clear which processes dominate in different types of remnants. We do not know what constitutes the seed population for the acceleration mechanism and how these particles become injected into the cycle. Although it is becoming increasingly evident that cosmic-ray protons have an important back-reaction on the SNR blastwave (see, e.g., Kang & Jones 1991), the observational consequences of cosmic-ray shock mediation have not been demonstrated. It is thus important to acquire observational data which can be compared directly with theoretical models.

While we cannot directly observe accelerated cosmic-ray nuclei within the remnant environment, we can gain some insight into the acceleration process from the nonthermal radiation emitted by relativistic electrons accelerated in SNRs. The electronic component, probably being dynamically unimportant to the overall shock evolution is generally treated as a test particle population in numerical simulations. As such, the electrons adapt passively to their environment and become an effective tracer of local shock and dynamical characteristics. The synchrotron spectral index, α (where $S_\nu \sim \nu^{-\alpha}$), reflects the average energy distribution among accelerated electrons within the beam solid angle.

We restrict ourselves here to consideration of only shell-type remnants, as they present the simplest case for studying Fermi acceleration. In these remnants, particles are presumably accelerated only in shocks and turbulent regions, as opposed to plerionic (Crab-like) remnants, where the bulk of the relativistic electrons are generated by a central pulsar. Shell remnants have typically been found to exhibit fairly uniform radio spectral indices (see, e.g., Scheuer 1984; Green 1988a). Recently, however, there have been reports of spatial spectral variations in a handful of shell remnants (see § 6.4).

These collective findings have prompted us to search for spectral index variations in other shell remnants. We selected three Galactic remnants with shell classifications from the SNR catalog compiled by Green (1988b), based on size, brightness, and declination considerations. SNRs G31.9+0.0 (3C 391), G39.2−0.3 (3C 396), and G41.1−0.3 (3C 397) were observed with the Very Large Array (VLA[1]; Napier, Thompson, & Ekers 1983) at $\lambda 6$ and 20 cm, and spatial distributions of spectral index, as measured between these two wavelengths, were derived therefrom. G31.9+0.0 proved to have too few independent beam areas with adequate signal-to-noise to facilitate a significant spectral variation study. However, the data for SNRs G39.2−0.3 and G41.1−0.3 did indicate spatially varying spectral indices.

We present here the evidence for spatial variations in shell SNRs G39.2−0.3 and G41.1−0.3, and possible interpretations of these variations in terms of models of particle acceleration. Section 2 reviews the existing body of knowledge on these two remnants, and § 3 introduces our new observations. In § 4 we discuss the image reconstruction and spectral distribution measurement procedures used in this study. Section 5 gives a description of the observed variations in α. Section 6 summarizes observations of spectral variations in other shell remnants and possible interpretations thereof.

2. BACKGROUND: EXISTING OBSERVATIONS OF G39.2−0.3 AND G41.1−0.3

2.1. *G39.2−0.3*

The classification of the SNR G39.2−0.3 has engendered a great deal of debate. The confusion arises due to the presence

[1] The Very Large Array is a facility of the National Radio Astronomy Observatory, operated by Associated Universities, Inc., under contract with the National Science Foundation.

of a substantial amount of central emission (see e.g., Caswell et al. 1982), reminiscent of Crab-like remnants, in addition to a shell-like structure which is evident in VLA observations (Becker & Helfand 1987; Patnaik et al. 1990). An *Einstein* IPC image of the source shows a similar morphology (Becker & Helfand 1987). As pointed out by Caswell et al. (1982), the integrated spectral index of G39.2−0.3 (he quotes $\alpha = 0.49$; [Clark & Caswell 1976], but see below) is more in keeping with the shell class (0.3–0.8) than with the plerionic class (0.0–0.3; Green 1988a). Becker & Helfand (1987) discuss the possibility of G39.2−0.3 being a composite-type remnant, with flat-spectrum emission generated by a central pulsar inside a steeper spectrum shell. Based on 1 hr integrations with the VLA in the C- and D-configurations at λ20 and 6 cm, however, they found no evidence for any spectral difference between the central emission and the shell, and thus concluded that the central emission was merely a segment of a patchy shell seen in projection.

Integrated flux density measurements for G39.2−0.3 have been compiled from the literature and brought to a common flux scale by Kassim (1989) and Patnaik et al. (1990). Both derive a spectral index of $\alpha = 0.4$ above 400 MHz and show a turnover below 100 MHz due to free-free absorption. Green (1991) quotes a steeper index of $\alpha = 0.6$.

The high-resolution (~8″), high dynamic range VLA observations of G39.2−0.3 presented by Patnaik et al. (1990) show a shell with an indication of filamentary structure (see their Fig. 3). Their D-array λ20 cm image (their Fig. 1) shows a rather unusual plumelike feature emanating from the northeast segment of the shell and curving around to the west. They estimate the spectral index of this plume to be $\alpha = -0.15 \pm 0.12$, which they point out is consistent with either optically thin thermal emission, or with a flat-spectrum nonthermal Crab-like source. No linearly polarized flux was detected at λ6 cm in the region of the plume down to a limit of ~5% (scaling their highest λ20 cm total intensity contour in the plume to λ6 cm by $\alpha = -0.15$). Another example of a spectrally flat "jet" or plume associated with a shell is found in SNR G332.4+0.1 (Roger et al. 1985). In this case, the spectral index in the shell varies between $\alpha = 0.45$ and 0.55 ± 0.05, while the base of the jetlike feature has $\alpha = 0.05 \pm 0.1$. Roger et al. suggest two possible models for the jet emission: synchrotron radiation from a Crab-like population of electrons accelerated by a central stellar remnant, or thermal recombination radiation from a preexisting neutral gas cloud which was ionized by the supernova event.

The D-array image of Patnaik et al. also shows the H II region NRAO 591 to the northwest of G39.2−0.3. To the southeast is the radio source 1901+053B, a strong source of IR emission (Becker & Helfand 1987) and probably also an H II region. Patnaik et al. suggest that dents in the lower flux density contours in the southeast part of the remnant may be morphological evidence that G39.2−0.3 and 1901+053B are interacting. No optical counterpart to the remnant has been detected. Clarke & Caswell (1976) estimate its age at ~2500 yr.

2.2. *G41.1−0.3*

As noted by Caswell et al. (1982), G41.1−0.3 is among the smallest, brightest, and apparently youngest known shell remnants in our galaxy. Based on the Caswell & Lerche (1979) Σ-D relationship, Caswell estimates its age to be 600 yr, and its diameter, 12.9 pc. In terms of surface brightness (at 1 GHz), it ranks fifth out of 99 remnants with clear shell classifications, as cataloged by Green (1991).

G41.1−0.3 has been imaged at subarcminute resolution by Caswell et al. (1982) and Becker, Markert, & Donahue (1985). Caswell noted, based on his 50″ resolution λ20 cm observations, that the remnant brightens in the direction of the Galactic plane. This is a characteristic common to many shell remnants (see, e.g., Caswell 1977; Shaver 1982) and is generally attributed to large-scale density gradients in the ISM. Caswell also pointed out that if G41.1−0.3 is truly significantly nonspherical, it is unique among the three youngest known remnants, Cas A, Tycho, and Kepler, which are all highly circular. The correlation of youth (brightness) and sphericity in shell remnants has been confirmed statistically by Shaver (1982). Eight arcsecond resolution "scaled array" VLA observations at λ6 and 20 cm by Becker et al. (1985) confirmed the fact that G41.1−0.3 is highly asymmetric. Their contour plots show it to have a semicircular projected morphology, with marked gaps in the shell limb brightening. Contrary to our findings, they saw no evidence for spectral index variations in their observations.

Kassim (1989) derives an integrated spectral index of $\alpha = 0.4$ for G41.1−0.3, with a turnover at frequencies less than 100 MHz. This turnover may be due to absorption by the H II region G41.1−0.2 which lies 7′ to the west of the SNR (Cersosimo & Magnani 1990). There is no evidence to suggest that the remnant and this H II region are directly interacting. Green (1991) quotes an integrated index of $\alpha = 0.48$.

An *Einstein* IPC X-ray image of G41.1−0.3 shows two central regions of enhancement (Becker et al. 1985), neither of which clearly correlates with any bright radio features. G41.1−0.3 has no optical counterpart.

3. NEW OBSERVATIONS OF G39.2−0.3 AND G41.1−0.3

3.1. *Observing Parameters and Calibration*

The new observations presented here were taken with the VLA in the scaled C-array (at λ20 cm) and D-array (at λ6 cm) configurations, yielding a resolution of ~14″ at each frequency. Details of these observations are given in Table 1.

Primary flux calibration was based on the Baars flux scale for 3C 48 (Baars et al. 1977, as modified in the 1990 VLA Calibrator Manual). Flux densities for 3C 48 of 15.78 and 5.61 Jy were assumed for frequencies 1452 and 4885 MHz, respectively. The phase calibrators used in C-array were 1819−096 for G41.1−0.3 and 1821+107 for G39.2−0.3; in D-array, 1821+107 was used for both remnants.

The observing bandwidths were chosen to yield less than 1% intensity loss due to bandwidth smearing at the edge of each remnant. Time-averaging smearing was negligible in comparison.

All data were self-calibrated in phase using standard VLA procedures.

TABLE 1

OBSERVING PARAMETERS

Frequencies (MHz)	Bandwidth (MHz)	Time per Source (minutes)	Array	Date
1452.....	25	179	C	1990 Dec 1
4885.....	50	255	D	1991 Mar 26

3.2. *New Total Intensity Images*

The new total intensity images of G39.2−0.3 and G41.1−0.3 at $\lambda 20$ cm are shown in Figures 1 and 2. The images presented in this section were reconstructed using the AIPS Maximum Entropy routine VTESS and have been corrected for primary beam attenuation. The gray-scale images have not been convolved, so as to accentuate the fine filamentary structures which define these two remnants. More detail on the image reconstruction techniques used in the spectral index determination is given in § 4.

3.2.1. *G39.2−0.3*

Figure 1*a* shows the filamentary nature of G39.2−0.3 in great detail. We can be confident that all structure apparent in this image is real, as it is replicated to fine detail at both $\lambda 6$ and 20 cm. This is true even of the regular graininess of the fainter interior regions, which looks very much like instrumental ripples. The fact that the positions and morphologies of these grains, and even the subtle brightness variations along filaments, are so very similar in the $\lambda 6$ and 20 cm images argues strongly against an instrumental origin for the mottling. The lower contrast filaments in the central region of the remnant are also found in both maps.

A few of the most highly defined filaments in G39.2−0.3 appear to almost completely girdle the remnant, with the exception of a few gaps. In this respect, G39.2−0.3 should be compared to the radio source G318.9+0.4 (Whiteoak 1990), which exhibits a central core of bright emission encircled by a series of elliptical arcs. There is a large-scale brightness asymmetry in the east-west direction across G39.2−0.3, the western half of the remnant having roughly twice the flux density of the east. The centrally enhanced emission is filamentary and mottled, much like the surrounding interior structure. As noted by Becker & Helfand (1987) and Patnaik et al. (1990), the central emission does not appear morphologically distinct from other parts of the shell. As displayed in Figure 1, the central structure appears to be part of a continuous elliptical annulus which includes the bright southwestern rim of the remnant. If this interpretation is correct, the central enhancement is most probably not located internally, within the shell.

Projecting out from the northeast edge of the remnant, one can see a very faint and narrow pencil-like portion of the "jet," or "plume," identified by Patnaik et al. (1990) (see the contour plot in Fig. 1*b*). This ridge defines the bottom limb of the plume and narrows the distance from the remnant. The plume itself, which arcs over north of the remnant, is visible in our images using different display transfer functions.

The radio source 1901+053B can be seen to the southeast of G39.2−0.3 in Figure 1*b*. Our observations do not lend any additional evidence to the supposition that these two sources are interacting, as proposed by Patnaik et al. (1990).

3.2.2. *G41.1−0.3*

Like G39.2−0.3, G41.1−0.3 is predominantly filamentary in nature. Again, all of the structure apparent in the $\lambda 20$ cm image, as displayed in Figure 2*a*, can be found in the $\lambda 6$ cm image as well. Filaments in the remnant interior (projected) define a cellular pattern, especially in the northwest corner. Although the mechanisms by which radio filamentation is formed in various types of SNRs are not well understood, the visual impression given by G41.1−0.3 is one of expanding and intersecting shock waves.

As pointed out by Caswell et al. (1982), there is a brightening along the northwestern face of G41.1−0.3, toward the Galactic plane. The remnant is extended in the direction perpendicular to the Galactic plane, with an axial ratio of almost 2:1. The flatness of the northeastern boundary of the remnant is suggestive of inhibited expansion in this direction. However, there is no significant brightening on this face, as might be expected to accompany enhanced compression.

4. SPECTRAL INDEX DISTRIBUTION DETERMINATION

The range in spectral indices we find in G41.1−0.3 and G39.2−0.3 is on the order of $\Delta\alpha \sim 0.2$, while typical errors in α in our measurements are 0.02–0.03. Since the spectral variations observed in these remnants are so subtle, we have taken special care to examine their robustness to instrumental and image reconstruction effects. The method used to reconstruct the images used in the spectral index distribution determination is explained in § 4.1. To verify that the variations observed have not been artificially generated by this specific reconstruction technique, the images have also been reconstructed via three additional methods, as discussed in § 4.2. In that the results from each method are qualitatively similar, we are confident that the observed spatial variations are not an artifact of the reconstruction process. The method used to extract spectral index measurements from the data is described in § 4.3, and a comparison of the different image reconstruction methods used is presented in § 4.4.

4.1. *Primary Deconvolution Strategy*

The process of image reconstruction in this experiment was complicated to some extent by somewhat unequal aperture coverage between the two observing bands. Enhanced antenna shadowing in the VLA D-configuration caused a preferential loss of short spacings at $\lambda 6$ cm. The $u - v$ range sampled at $\lambda 20$ cm was 0.15–16 kλ, while at $\lambda 6$ cm, the minimum baseline was 0.4 kλ. In comparison with integrated spectra published by Kassim (1989), we have detected 93% and 37% of the total flux density of G39.2−0.3 at $\lambda 20$ and $\lambda 6$ cm, respectively, with 71% and 38% detections for G41.1−0.3. At $\lambda 20$ cm we should have adequate flux for a reasonable reconstruction of both remnants. However, at $\lambda 6$ cm the largest spatial scales are somewhat undersampled. The goal of our mapping strategy was to equalize the $u - v$ coverage at both bands, while providing the reconstruction routine with as much information as possible concerning the large-scale structure in the remnants. To this end we adopted the following two-stage procedure as our primary mapping technique.

In the first stage, each remnant was mapped at $\lambda 20$ cm using the full sampled $u - v$ range of 0.15 to 16 kλ. These images were deconvolved using the AIPS Maximum Entropy algorithm VTESS (see, e.g., Cornwell & Evans (1985), Narayan & Nityananda (1986) for discussions of Maximum Entropy reconstruction). VTESS was run to convergence based on a specified noise level of 0.1 mJy beam^{-1}, determined from maps of Stokes parameter V. The output $\lambda 20$ cm maps were convolved to 200″, corresponding to a maximum $u - v$ spacing of ~ 1 kλ.

These low-resolution $\lambda 20$ cm maps were used as the default images in the second stage of deconvolution with VTESS to produce the final $\lambda 20$ and $\lambda 6$ cm reconstructions. At $\lambda 6$ cm, the default images were corrected for $\lambda 20$ cm primary beam attenuation, scaled down according to an estimate of the integrated spectral index ($\alpha = 0.5$ was used for both remnants, a

1993ApJ...408..514A

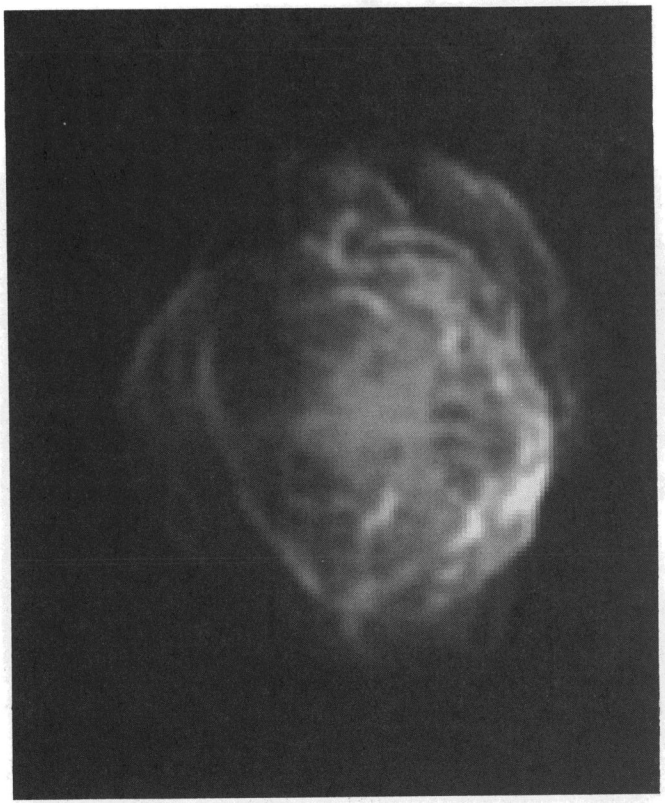

FIG. 1*a*

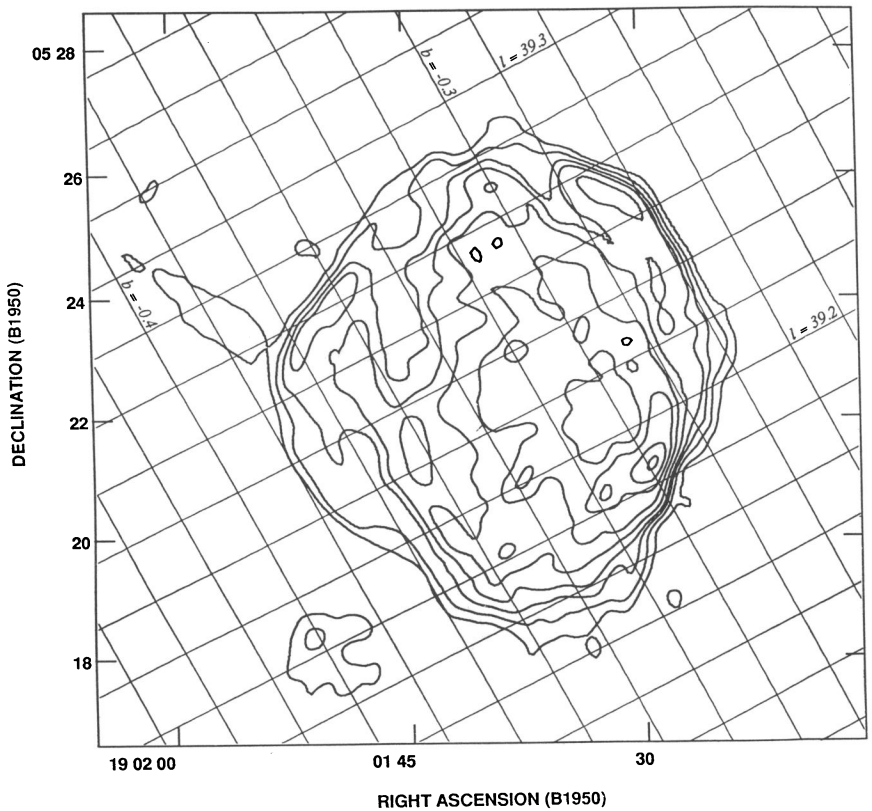

FIG. 1*b*

FIG. 1.—(*a*) Gray-scale total intensity map of G39.2−0.3 at λ20 cm. This image, reconstructed via the Maximum Entropy routine VTESS, has not been convolved, so as to emphasize the filamentary nature of the remnant. (*b*) A contour diagram of the image shown in (*a*), convolved to a resolution of 15″.5. A Galactic coordinate grid is included to show the orientation of the remnant with respect to the Galactic plane. Contours are at levels 6, 10, 15, 20, 30, 45, 60, 75, and 90 mJy beam^{-1}.

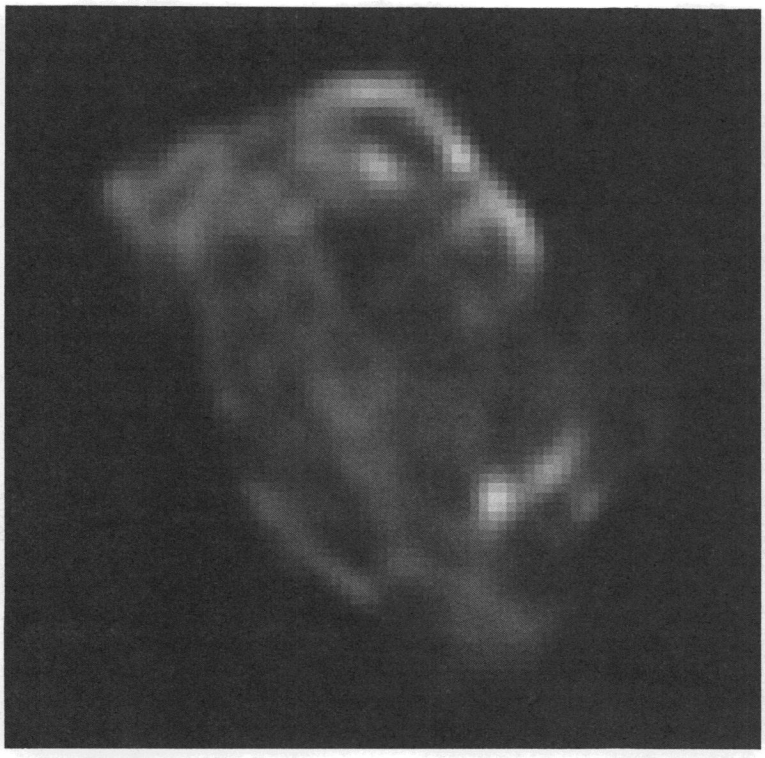

FIG. 2a

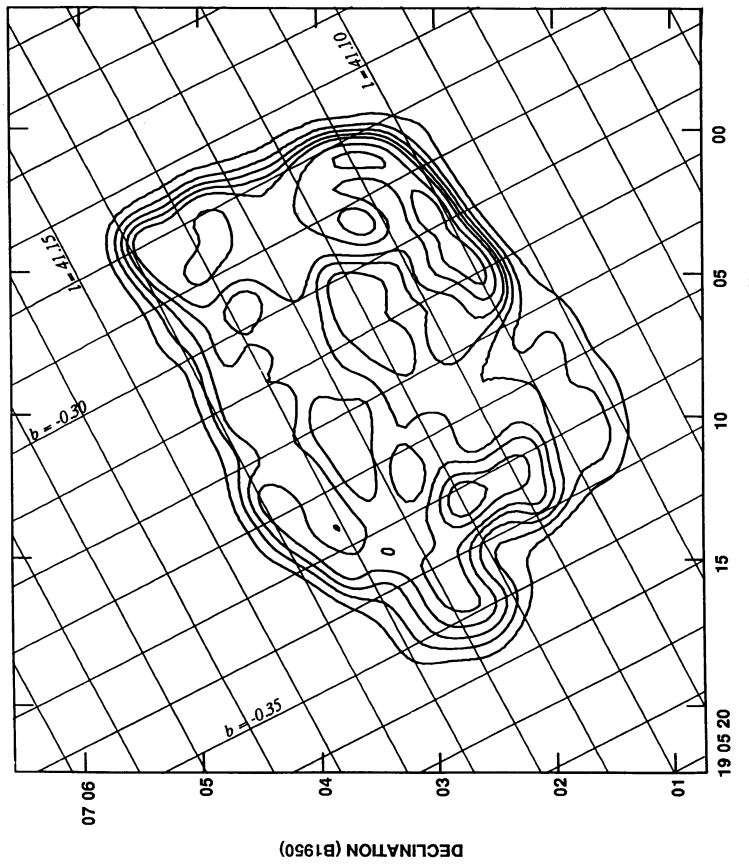

FIG. 2b

FIG. 2.—(*a*) Gray-scale total intensity map of G41.1 −0.3 at λ20 cm. (*b*) A contour diagram of the image in (*a*), convolved to a resolution of 15″.5. Contours are at 20, 40, 60, 80, 100, 140, and 180 mJy beam^{-1}.

compromise between various indices quoted in the literature), and then attenuated by the $\lambda 6$ cm primary beam pattern.

For the second-stage runs of VTESS, the input maps at each band were constructed using a restricted $u - v$ range, determined by the sampling at $\lambda 6$ cm (>0.4 kλ). VTESS was run to convergence with specified noise levels of 0.1 mJy beam^{-1} at $\lambda 20$ cm, and 0.05 mJy beam^{-1} at $\lambda 6$ cm, using the 200″ maps described above as defaults. In doing this we were, in effect, requesting that the reconstructed images at both bands be as similar as the sampled data would allow on spatial scales larger than 200″. The spatial frequency coverage is matched on smaller scales, thus the resultant images should be directly comparable.

All images used for spectral index measurement have been convolved to a common resolution of 15″.5 and include the residuals from the deconvolution procedure. Each image has been corrected for primary beam attenuation. With this method we have reconstructed, to within 8%, the flux densities at $\lambda 20$ cm predicted by the integrated spectra of Kassim (1989). The reconstructed flux densities at $\lambda 6$ cm for G39.2−0.3 and G41.1−0.3 are within 98% and 93%, respectively, of what is expected from the $\alpha = 0.5$ scaling imposed between the $\lambda 6$ and 20 cm default images. The fact that VTESS converged given these defaults indicates that the assumed scaling is reasonable.

4.2. *Comparative Reconstruction Techniques*

To study the effects of $u - v$ range restriction and the particular choice of default image, the $\lambda 6$ cm images were also reconstructed via two variations on the Maximum Entropy strategy discussed above. In the first comparison, a *full* resolution VTESS output $\lambda 20$ cm image (appropriately scaled and attenuated) was used as the default image in the $\lambda 6$ cm reconstruction. No $u - v$ range restrictions were imposed at either wavelength. This method addresses two objectives: the large-scale structure sampled in the $\lambda 20$ cm data is passed on to the $\lambda 6$ reconstruction through the default, and, on all spatial scales, the final images are required to have as uniform a scaling between bands as the data will allow—any resultant scaling variations must truly be due to a strong signal in the data.

As a second comparison, no default image was used at either band. Both bands were reconstructed completely independently, using no $u - v$ restrictions.

Finally, to verify that the observed spectral variations are not artifacts generated by some nonlinear peculiarity of the Maximum Entropy Method, the dirty maps for both remnants at both frequencies were also reconstructed with an adaption of the CLEAN algorithm (Högbom 1974). CLEAN in its standard form quickly picks out components in the negative bowls which surround the sources as a result of missing short $u - v$ spacings. To avoid this, a constant positive offset was added to each map, of magnitude slightly greater than the absolute value of the most negative pixel in the map. These "forced positive" maps were CLEANed down to a level of $\sim$(offset + 3 σ), where σ is the noise measured in a map of Stokes V. The offset was then subtracted from the CLEANed images. Although the quality of the CLEANed maps is not as high as that obtained from Maximum Entropy restoration, the resultant spectral distributions are quite similar (see § 4.4).

4.3. *Method for Measuring Spatial α-Distribution*

In the § 4.4 we will demonstrate that the observed spectral variations are not tied to a specific image reconstruction technique. However, radio spectral indices can still be easily corrupted by low-level background variations. In interferometric data, these variations may be a result of incomplete spatial coverage, for example, negative bowls, or an incomplete reconstruction of large-scale Galactic background emission. Local additive "biases" of this type can yield false variations in maps of apparent spectral index, $\alpha_{\rm app} = \ln(S_1/S_2)/\ln(\nu_1/\nu_2)$. In addition, *real* variations in background/foreground emission may cause spatial changes in the observed spectral index, even if the object of interest has a constant spectral value. This problem is highlighted in Figure 3, which shows a map of the quantity $(S_{\lambda 20\ {\rm cm}} - XS_{\lambda 6\ {\rm cm}})$ for G39.2−0.3, where $X = 1.84$ is the average scale factor between the $\lambda 6$ and 20 cm maps. The flat spectrum plume to the northeast can be seen to extend, in projection, inside the remnant shell. The H II region to the south is also contaminating the remnant's spectral indices.

In order to reduce the effects of either instrumental or real contamination from additive biases, it is preferable to determine spectral index distributions from the *slope* of (S_1 vs. S_2) within specified regions of the source, as opposed to the *ratio* S_1/S_2. If regional linear regressions are computed between intensities at two frequencies, allowing a floating offset, any additive biases which are constant over the region in question are eliminated. If the background varies on scales smaller than this, the effect will be incorporated into the regression error, and thus is properly accounted for. Real variations in α within a box are treated, according to this method, as an additional source of noise; the linear fit, however, should be a good representation of the local average spectral index. Note that this method, in effect, spatially filters out emission on scales larger than the specified region, thus one is measuring only spectral indices associated with small-scale features (features whose brightnesses vary significantly within the region).

The gray scales in Figures 4*a* and 5*a* show distributions in spectral index in G39.2−0.3 and G41.1−0.3, as measured in the following way. A box defining the regression area was slid over each remnant in two dimensions at one pixel increments. At each position we computed a linear regression between the intensities at $\lambda 6$ and 20 cm in pixels lying within the box, retaining both the slope and the offset of the best-fit line. To avoid a bias in our fits imposed by the higher noise at $\lambda 20$ cm, we averaged the slopes obtained from regressions of ($S_{\lambda 6\ {\rm cm}}$ vs. $S_{\lambda 20\ {\rm cm}}$) and ($S_{\lambda 20\ {\rm cm}}$ vs. $S_{\lambda 6\ {\rm cm}}$). The local spectral index, $\alpha_{\rm reg}$, is computed from this average slope.

To eliminate all off-source background points from the fits, pixels in the input maps were blanked where $S_{\lambda 6\ {\rm cm}} < 4$ mJy beam^{-1} for G39.2−0.3 and <10 mJy beam^{-1} for G41.1−0.3. The box sizes used were chosen to be on the scale of the spatial variations evident in maps of $\alpha_{\rm app}$, based on the presumption that these variations might be merely bias-induced. Sampling every third pixel within the box ($\sim$1 sample/beam) yielded 25 independent points per fit for G41.1−0.3 and 49 points for G39.2−0.3, for fully unblanked regions. The spectral variations in $\alpha_{\rm reg}$, apparent in Figures 4*a* and 5*a*, are, in general, qualitatively similar to those found in maps of $\alpha_{\rm app}$. However, the distribution of $\alpha_{\rm reg}$ is considerably smoother due to the spatial averaging inherent in the regression method and the reduction of spectral contamination.

The spectral indices shown in Figures 4*a* and 5*a* are somewhat correlated with the local offsets derived in the regressions, in the sense that b (where $S_{\lambda 20\ {\rm cm}} = mS_{\lambda 6\ {\rm cm}} + b$) increases with flattening $\alpha_{\rm reg}$ (decreasing m). This is because there are a series of choices of m and b which are linearly related and yield a similar goodness of fit. This ambiguity increases the error in

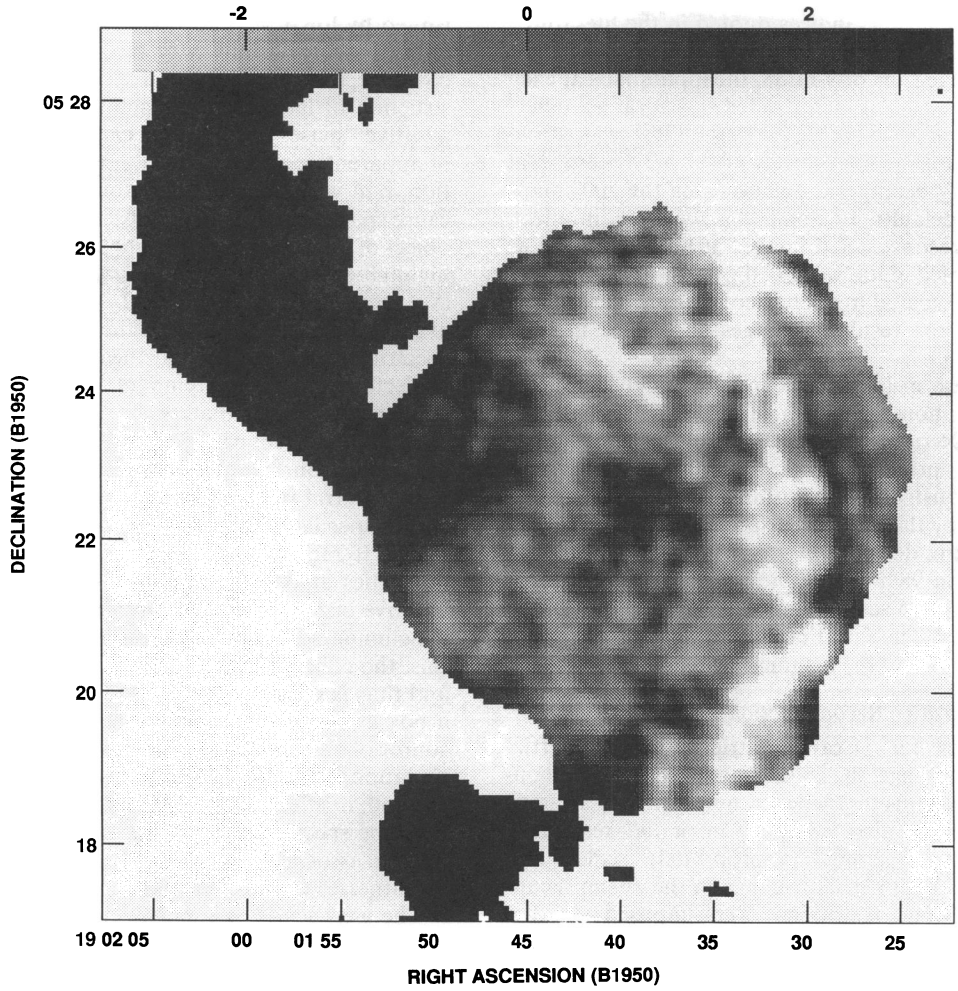

FIG. 3.—A gray-scale map of the quantity ($S_{\lambda 20\,\mathrm{cm}} - XS_{\lambda 6\,\mathrm{cm}}$) for G39.2−0.3, where $X = 1.84$ is the mean scaling factor between the $\lambda 6$ and $\lambda 20$ cm maps of the remnant. The range in flux densities displayed is −3 to 3 mJy beam^{-1}.

our determination of α_{reg}. To quantify this effect, we have examined the rms residuals of linear fits with a range of m and b values for the regions outlined in Figures 4*a*, 4*b*, 5*a*, and 5*b*. These regions were selected as being representative of the major spectral variations evident in the α_{reg} maps. The contours plotted in Figures 4*c* and 5*c* define the 90% confidence limits for $\alpha_{reg}(m)$ and b, as determined by the χ^2 statistic. The significance of spectral variations between regions can be evaluated by projecting these contours onto the α_{reg}-axis (see Tables 2 and 3).

4.4. *Comparison with Other Reconstruction Techniques*

Figures 6*a* and 6*b* are comparisons of α_{reg} measured in several regions in G39.2−0.3 and G41.1−0.3 from maps made via the four reconstruction techniques discussed in §§ 4.1 and 4.2. The correlation is quite good for both remnants, and the spread is consistent with the errors in α_{reg} determined from the scatter about the best-fit line for each box. We can therefore be confident that these spectral variations are not created in the image reconstruction process itself— by differences in $u - v$ coverage, or by nonlinear aspects of Maximum Entropy. Note that the primary reconstruction technique yields the smallest errors by a significant margin.

5. SPECTRAL INDEX DISTRIBUTIONS

5.1. *G39.2−0.3*

Figure 4*a* shows the spatial distribution of α_{reg} in G39.2−0.3. Spectral indices displayed in this image range

TABLE 2

G39.2−0.3

SPECTRAL INDEX MEASUREMENTS

Region	α	Error limits (90% confidence)
A	0.39	+0.10, −0.05
B	0.55	+0.03, −0.03
C	0.58	+0.04, −0.05
D	0.49	+0.07, −0.05
Whole remnant	0.53	

TABLE 3

G41.1−0.3

SPECTRAL INDEX MEASUREMENTS

Region	α	Error limits (90% confidence)
A	0.66	+0.03, −0.04
B	0.51	+0.05, −0.03
C	0.60	+0.02, −0.03
D	0.52	+0.06, −0.06
E	0.59	+0.05, −0.04
Whole remnant	0.59	

1993ApJ...408..514A

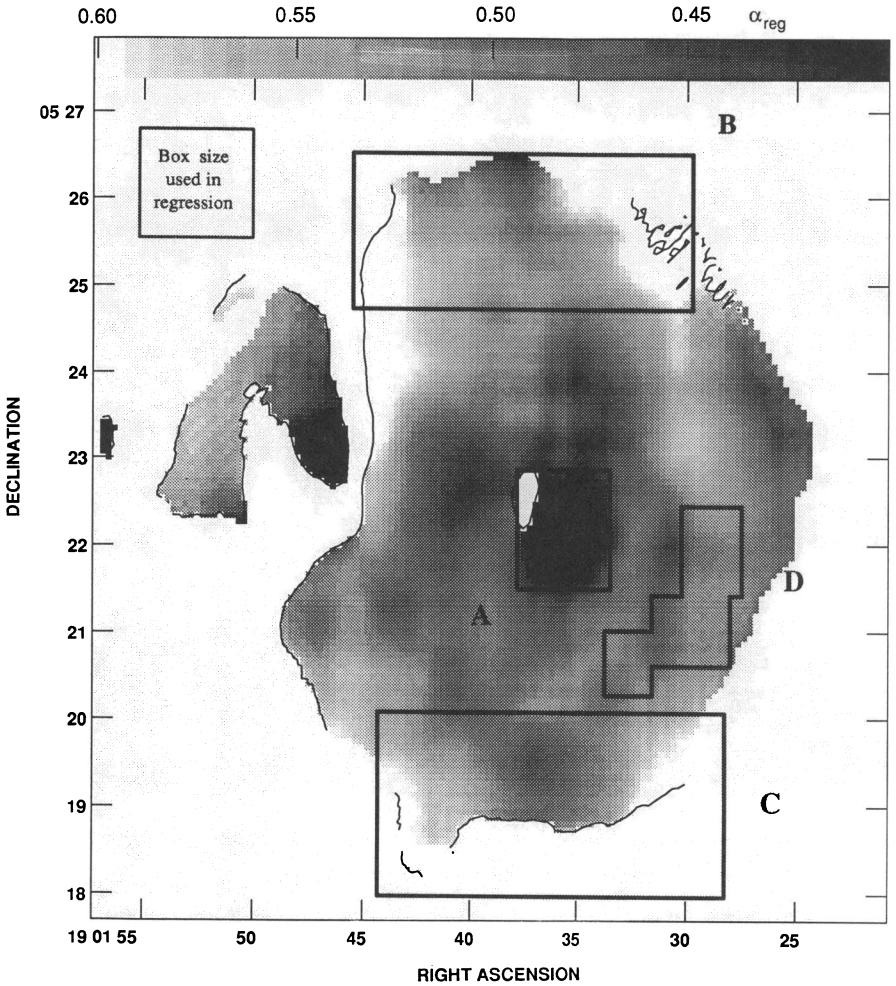

FIG. 4*a*

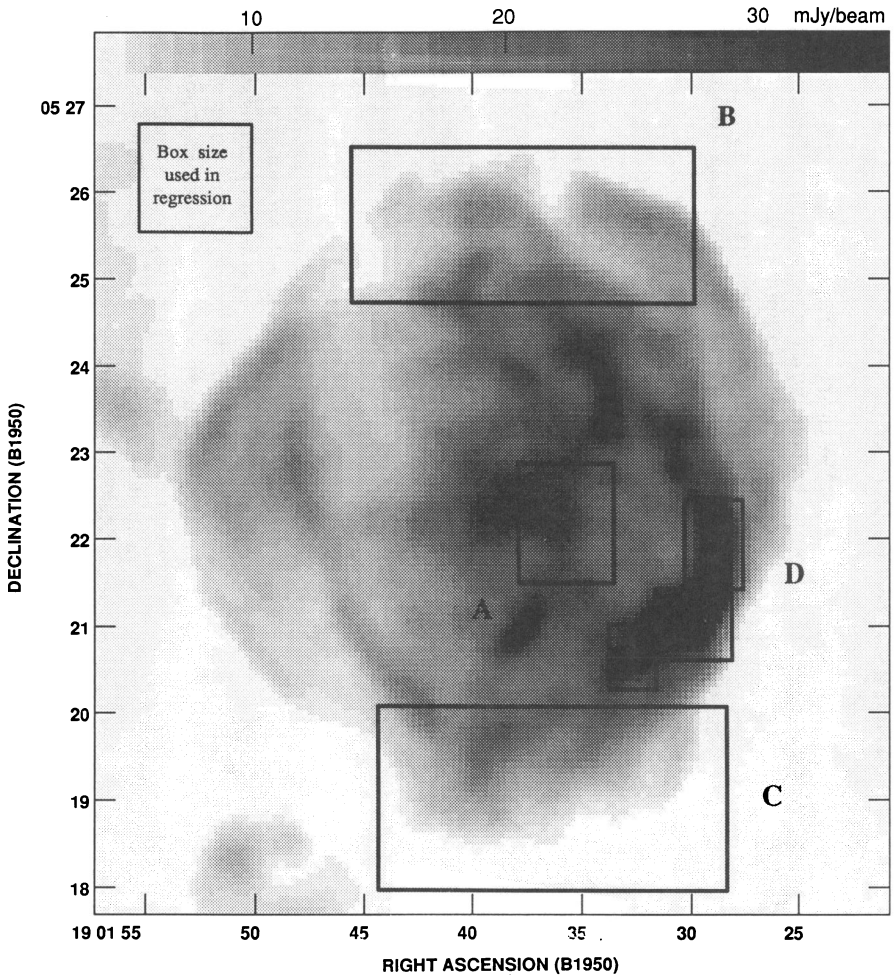

FIG. 4*b*

FIG. 4.—(*a*) Map of α_{reg} for G39.2−0.3. Pixels with errors $\delta\alpha_{reg} > 0.03$ have been blanked (blanked pixels in the remnant interior are enclosed within a contour line). The overlaid boxes demarcate regions referred to in (*c*). (*b*) 15″.5 resolution gray-scale total intensity image of G39.2−0.3, deconvolved via the primary reconstruction technique discussed in § 4.1. (*c*) Contours of constant χ^2 in α-offset space for G39.2−0.3. These contours define the 90% confidence levels for linear fits to ($S_{\lambda 20\ cm}$ vs. $S_{\lambda 6\ cm}$). Small crosses denote the most probable values for α and offset for each region. The large cross represents the α and offset measured for the remnant as a whole.

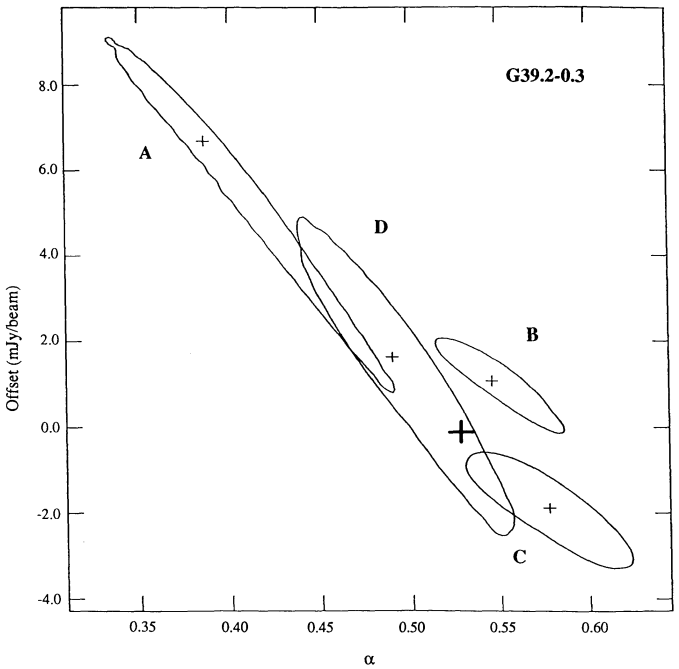

FIG. 4c

between 0.4 and 0.6 (only pixels with regression error $\delta\alpha_{reg} < 0.03$ have been plotted). The spectral index and offset obtained from a linear regression of all points in the remnant (excluding the plume) are indicated in Figure 4c by the large cross. This "mean" spectral index of $\alpha = 0.53$ is considerably steeper than the $\alpha = 0.4$ derived by Kassim (1989). This is not surprising, as we have assumed an integrated spectral index of 0.5 in creating the default image for the $\lambda 6$ cm Maximum Entropy deconvolution. We have also isolated the flat plume and southern H II region from our estimate.

Region A (as outlined in Figs. 4*a* and *b*) stands out in this distribution as being uniformly flatter than other regions in the remnant, with $\alpha_{reg} = 0.39$. It is flatter than the northern and southern parts of the remnant (regions B and C, with $\alpha_{reg} = 0.55$ and 0.58, respectively) at a very high level of confidence (as indicated by lack of overlap of the 90% confidence contours in Fig. 4*c*, when projected onto the α_{reg} axis). Comparing Figures 4*a* and *b*, it is apparent that the region with the flattest α_{reg} does not coincide with the central radio concentration, but rather lies to the west by $\sim 30''$. This displacement is robust to a variety of regression window sizes and cutoff levels.

Region D is the brightest feature in the G39.2−0.3 and is a segment of the western annular enhancement. It is somewhat flatter than the remnant mean (at $\sim 90\%$ confidence, see Fig. 4*c*), having $\alpha_{reg} = 0.49$, yet steeper than region A. There are other moderately flat structures apparent in the α_{reg} map; most of these originate in regions of low signal and are therefore not very reliable.

As discussed earlier, maps of α_{app} show contamination in the southeastern part of the remnant by the adjacent H II region, and the eastern filaments are flattened due to the presence of the flat plume (see Fig. 3). The regression method of determining spectral indices has filtered out the large-scale flat emission to a large extent, or has tagged the contaminated emission with large errors in α. The flat region in Figure 4*a*, near $19^h01^m47^s$, 05°23′, is presumably an artifact of this corruption and may not be intrinsically flat.

Figure 3 clearly shows that the plume extends inside the projected boundaries of the remnant. The base of the plume in this image appears to point back to the central condensation. It is not clear, however, whether the plume originates interior to the shell, or whether it is emerging from the front or back face.

5.2. *G41.1−0.3*

The distribution of α_{reg} for G41.1−0.3 is shown in Figure 5*a*. The spectral indices displayed here (for pixels with $\delta\alpha_{reg} < 0.03$) range between 0.5 and 0.7. The α_{reg} derived for the remnant as a whole is 0.59, again steeper than Kassim's (1989) integrated spectral index of 0.4. As with G39.2−0.3, this may reflect both the scaling assumed in the deconvolution procedure and reduced spectral contamination by the adjacent H II region, obtained at higher resolution.

The most pronounced spectral feature in Figure 5*a* is the steep area in region A, with $\alpha_{reg} = 0.66$. This region contains parts of the bright western edge of the remnant and some fainter interior filaments—there is no obvious signature in total intensity distinguishing this region from other parts of the remnant. We find that the positioning of this steep region is not dependent on the choice of window size or minimum flux density cutoff used in the regression. Examining the contours in Figure 5*c*, we can say that region A is steeper than the remnant mean at a confidence level of greater than 90%.

Region B lies along the northeastern edge of the remnant. With $\alpha_{reg} = 0.52$, it is flatter than the remnant mean to a very high level of confidence, as evidenced in Figure 5*c*. This region of flattening is coincident with, but not limited to, a filamentary feature in total intensity (see Fig. 5*b*). A similarly flat α_{reg} is found in region D, in the remnant (projected) interior. This region, however, has a very low surface brightness, so the errors associated with α_{reg} are large. It is fair to say that region D is flatter than region A and the remnant mean.

Region C, containing the brightest filament in the remnant, shows no internal spectral variations, and its $\alpha_{reg} = 0.60$ is consistent with the remnant mean. Region E, corresponding to the bright curved filament in the southwest corner of the remnant, has $\alpha_{reg} = 0.59$, also consistent with the mean. The large range in acceptable spectral index and offset evident in Figure 5*c* indicates there is probably a notable variation in zero-level through this region.

Region A happens to coincide with one of the two X-ray enhancements found in the *Einstein* IPC image of G41.1−0.3, as contoured by Becker et al. (1985). The other X-ray bright region overlaps the flat northeastern remnant edge in region B. Note, however, that the positional uncertainty for the IPC instrument is $\sim 45''$.

6. INTERPRETATION OF SPECTRAL VARIATIONS

6.1. *Possible Interpretations*

Explanations for spectral variations observed in shell remnants generally invoke spatially dependent particle acceleration or bends in the relativistic electron energy spectrum, or a combination thereof. The most commonly discussed models are reviewed here.

Different variations of particle acceleration theory predict different behaviors for spectral index as a function of local shock compression ratio. In the first-order Fermi model, stronger shocks yield flatter indices, up to an $\alpha = 0.5$ limit (e.g., Bell 1978). First-order acceleration in the test particle limit

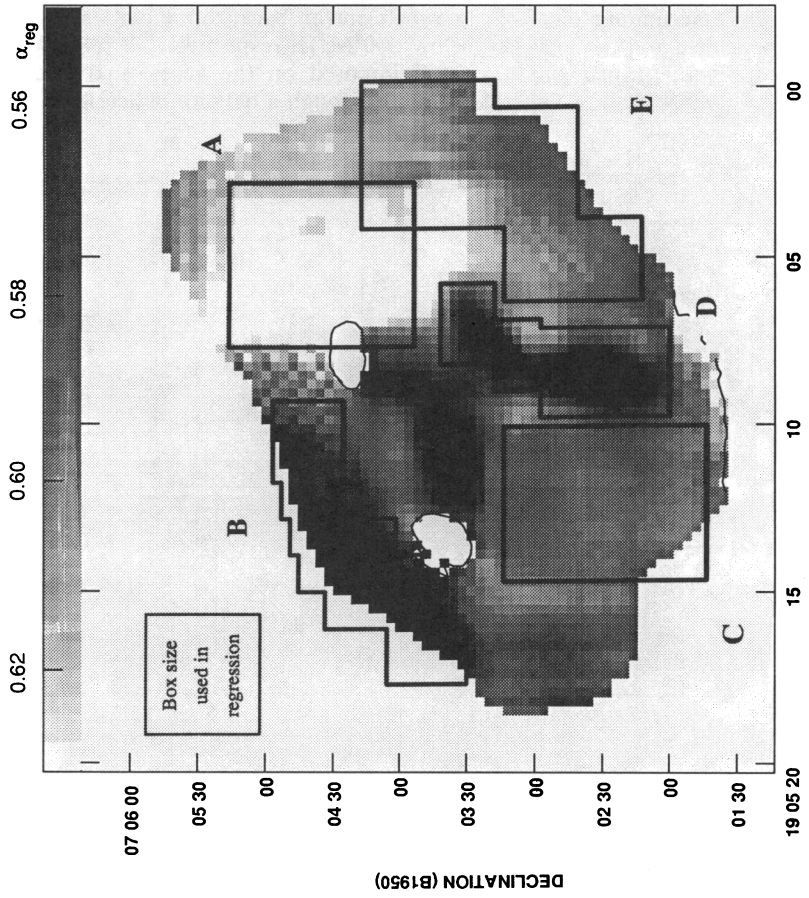

FIG. 5a

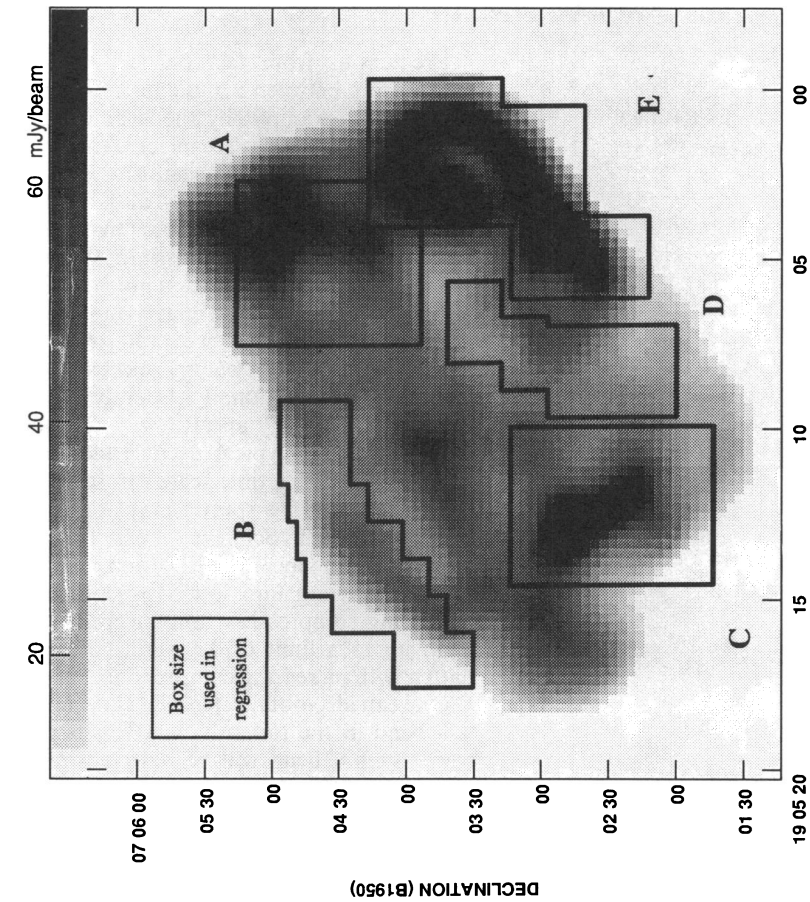

FIG. 5b

FIG. 5.—Analogous to Fig. 4, for G41.1−0.3

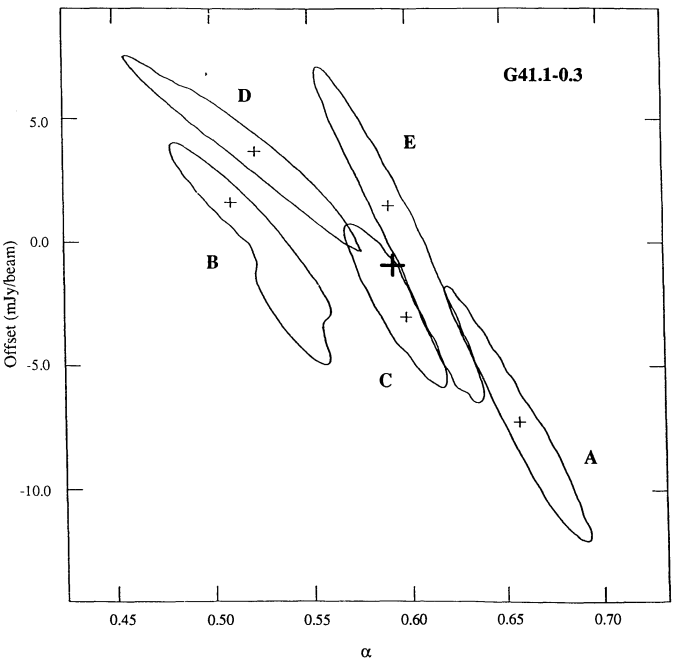

FIG. 5c

predicts, in the simplest scenario, that higher emissivity regions in a synchrontron source should be spectrally flatter. Note, however, that significant spectral variations are expected only for low Mach number shocks ($M \lesssim 10$); much lower than those predicted for typical Sedov remnant blastwaves. Nevertheless, any observed correlation between spectral index and synchrotron emissivity would indicate some relationship between the mechanisms responsible for determining local electron spectra and those creating magnetic field and/or particle density enhancements (e.g., shock compression or turbulent field amplification).

Predictions from test particle theory for the functional relationship between α and emissivity are, unfortunately, complicated, for example, by the issue of injection efficiency. The rate at which particles are injected from a thermal pool into the relevant acceleration mechanism may depend on, amongst other things, shock velocity and magnetic field orientation with respect to the shock front. Injection efficiency can therefore affect the observed emissivities in ways not considered in simple first-order acceleration models.

To predict the detailed effects on α of including second-order acceleration processes, we need to know the shape of the underlying turbulent energy spectrum—a difficult parameter to obtain, observationally. Eilek & Henriksen (1984) suggest that particle energy spectra will approach a power-law distribution over a typical particle lifetime. Dickel et al. (1989) point out that this time scale can be longer than the remnant age, thus power-law spectra may not be expected from second-order processes. Schlickeiser & Fürst (1989), assuming a momentum-independent diffusion coefficient, predict that for shocks traveling into low-β plasmas (where $\beta = 8\pi nkT/B^2$), increasing compression ratio steepens the synchrontron spectrum up to a limit of 0.5, while for high-β plasmas, spectra flatten with increasing compression.

One can also obtain spatially varying spectral indices if there is a bend in the radiating electron population's energy spectrum. Such a bend will be reflected in the synchrotron spectrum, where the observed break frequency is dependent on the local magnetic field strength. De Noyer (1974) lists three mechanisms for obtaining broken energy spectra: synchrotron losses (probably not important in the lifetime of an SNR, unless they occur at very early stages), an injection population derived from the Galactic cosmic-ray pool, which appears to have an intrinsically broken spectrum as evident in the Galactic synchrontron background (with $\alpha \sim 0.9$ and 0.4 above and below 200 MHz, respectively; Bridle 1967), or a high-energy cutoff imposed on the accelerated electron population, for example, through a balance of acceleration and diffusion time

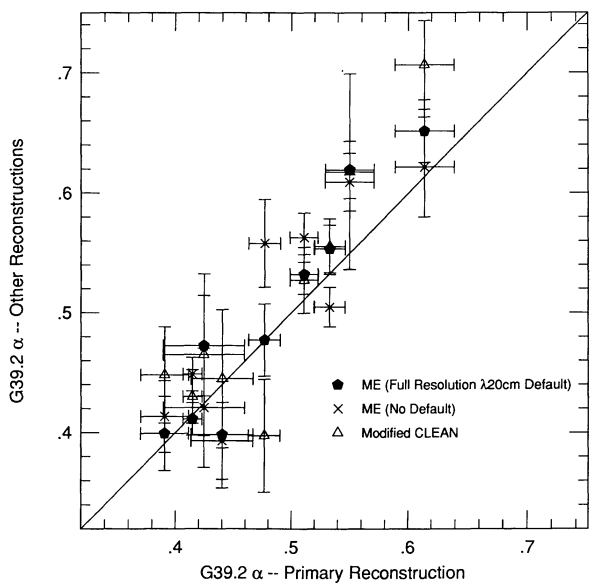

FIG. 6a

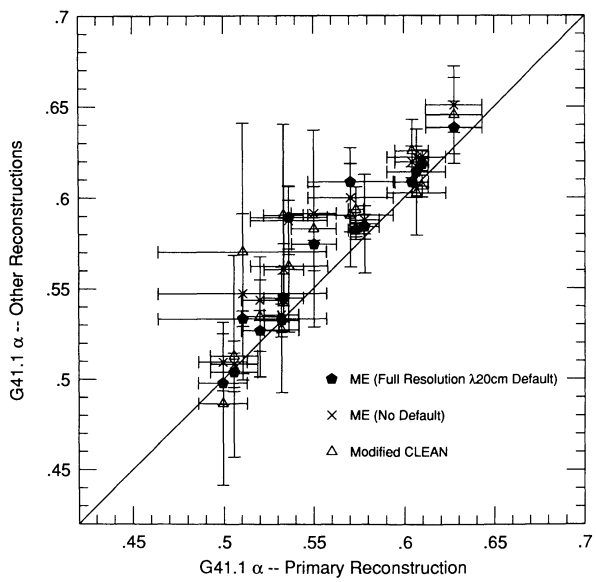

FIG. 6b

FIG. 6.—Comparison of spectral indices derived from maps of G39.2−0.3 reconstructed through the four different deconvolution techniques discussed in §§ 4.1 and 2. (*b*) Comparison of deconvolution methods for G41.1−0.3.

scales. Each of these mechanisms produced a *convex* synchrotron spectrum, that is, one that steepens at high energies. Thus a compression of fields and particles will yield flat spectra in high compression regions, where the break is shifted to high frequencies, and steep spectra in the more diffuse emission. Convex bends have been observed in remnants S 147 and the Cygnus Loop. However, strong questions have been raised as to whether these bends are real or merely instrumental artifacts (see, e.g., Green 1990).

Strongly cosmic-ray-mediated shocks can produce *concave* particle energy spectra, if the diffusion lengths of the electrons increase with energy (e.g., Ellison & Reynolds 1991). In these shocks, the cosmic-ray pressure decelerates the inflow in front of the shock, and thus decreases the compression ratio across the discontinuity. Lower energy particles, with shorter mean free paths, feel this reduced compression and thus are accelerated less strongly, while more energetic particles, with greater mean free paths, diffuse farther and see the full flow velocity change. Total compression ratios greater than 4 can be obtained, as the adiabatic index is altered from $\gamma = 5/3$ by the high-energy particles (Kang & Jones 1990). The behavior of emissivity as a function of spectral index in a cosmic-ray-mediated shock, however, is difficult to predict. It depends on, among other things, the prescribed function of diffusion length scale with particle energy—a function which has not yet been determined self-consistently for time-dependent acceleration at spherical shocks.

In some cases it can be argued that a given spectral variation may be due to contamination by an object unrelated to the SNR (e.g., a line-of-sight H II region). In interferometric observations, there is an upper limit to the angular size of possible contaminating sources due to the lack of short baselines. If spectral indices are determined through linear regressions, emission components with spatial scales larger than that of the regression box are effectively filtered out. In our observations, we are insensitive to features greater than 7′ (baseline limit) and greater than 1′ (regression limit).

6.2. *G39.2−0.3*

If the brightening in the western half of G39.2−0.3 is due to the blastwave impinging on a denser part of the interstellar medium, we might expect flatter indices to accompany the higher Mach number shocks which develop inside the cloud. The annular enhancement in shell brightness, however, does not stand out as a distinct feature in the map of α_{reg} in Figure 4*a*. In addition, the brightest filament in the southeast shows a spectral index similar to those of many fainter filaments in the remnant. Indeed, there is no apparent correlation between α and emissivity in G39.2−0.3. Assuming uniform injection efficiencies, if variations in emissivity in this remnant are due only to variations in local magnetic field strength, we cannot be viewing a single curved electron spectrum.

The possibility remains that the localized flattening in region A, as shown in Figure 4*a*, may be due to a foreground or background contaminating source. Such a source would have to have spatial brightness variations on scales less than 1′, or it would have been filtered out in the regression process. A map of rotation measure across the remnant would help to clarify the question of contamination by a spectrally flat, ionized medium. The source of potential contamination may also lie internal to the remnant; for example, a young plerionic nebula surrounding a hitherto undetected pulsar.

Perhaps the main question concerning the interpretation of the spectral variations observed in G39.2−0.3 is whether the central flattening and the flat plume are related phenomena. If the plume represents a shock breakout from the eastern half of the remnant, it is unlikely that region A is being contaminated by the flat plume material, due to the relative displacement of the two features. Another possibility is that this flat region indicates a central power source responsible for beam generation. Spectral studies of other SNRs with plumes would be useful for comparison purposes.

6.3. *G41.1−0.3*

As with G39.2−0.3, the spectral variations observed in G41.1−0.3 do not lend themselves to a straightforward, consistent interpretation, given the models discussed in § 6.1. It is not clear, for example, that the synchrotron spectra are tied to local shock conditions. The expansion of the northeastern face appears to have been inhibited by some external agent, based on its flat morphology. It may be that the SNR shock wave is encountering an external density enhancement in this direction. The northern face does exhibit flatter spectra, as might be expected for a higher local Mach number. However, there is no accompanying strong enhancement in emissivity along this edge. G41.1−0.3 has steep spectra which may be associated with the marked brightening along the northwestern edge, in the direction of the Galactic plane. It does not appear, however, that the steepening is in fact directly tied to features in total radio intensity; the steep region to the northwest spans bright and faint parts of the remnant.

It does not seem likely that the variations observed in G41.1−0.3 are due to a single curved electron energy spectrum viewed in regions of varying magnetic field. In the simplest case, a single energy spectrum with convex curvature, would yield flatter spectra in regions of higher emissivity, contrary to what is observed. A concave curvature cannot explain the filaments in the remnant that are fainter than the northeastern filament and yet steeper. Indeed, there is no consistent relationship between minimum energy or pressure magnetic field strength estimates for filaments in regions A, B, C, and E (assuming the filaments are cylindrically symmetrical) and their average α_{reg}. A single curved particle spectrum would predict some monotonic relationship between these parameters.

We must also consider contamination by an intervening source as an explanation for the localized steepening observed in G41.1−0.3. The only other large-scale source detected in these observations is the H II region to the west of the remnant—any resulting spectral confusion would serve only to *flatten* the spectra along the western edge. Any external diffuse emission lying in projection within the edges of the remnant is filtered out in the regression algorithm, if it is constant over spatial scales larger than 1′.

6.4. *Other Shell Remnants with Reported Spatially Varying Radio Spectra*

In working toward a unified picture of spatial spectral index variations in shell remnants, we must place the observations discussed here in the context of other remnants which have been reported to exhibit spectral variations. A basic overview of this set of remnants is given below.

6.4.1. *G33.6+0.1*

The radio morphology of G33.6+0.1 consists of an outer, somewhat asymmetric shell encircling a series of bright fila-

ments resembling concentric interior shells (Velusamy, Becker, & Seward 1991). Green & Dewdney (1992) present evidence to suggest that G33.6+0.1 is interacting with a nearby molecular cloud. They estimate the remnant's age at several thousand years, based on its size and asymmetric morphology.

From VLA observations at 327 and 1500 MHz at 1′ resolution, Velusamy et al. (1991) obtain spectral indices of ~0.6–0.75 in the remnant—Kassim (1989) and Green (1991) both report an integrated index of 0.5 for this source. Comparing intensity profiles through 1.5 and 5 GHz VLA maps, Velusamy et al. derive $\alpha = 0.4$ as representative of the interior rings, flatter than that of the diffuse emission. A flatter interior index, coupled with the centrally peaked X-ray and radio morphologies observed in G33.6+0.1, suggest a plerion embedded inside a shell; however, no evidence for a pulsar associated with this remnant has yet been found.

6.4.2. *IC 443*

The morphology of SNR IC 443 can be characterized as that of an "adolescent"-aged (~10^4 yr) remnant expanding into a nonuniform density environment (e.g., Parkes 1977; Mufson et al. 1986). The asymmetry between the relatively compacted, small radius of curvature northeastern rim and the fainter, radially larger southwestern part of the remnant is attributed to the interaction of IC 443 with a nearby H I cloud (De Noyer 1977). Duin & van der Laan (1975) found that there is a very good spatial correlation between optical filamentation in IC 443 and small-scale radio structure, especially in the radio-bright northeastern part of the shell.

Green (1986), comparing observations of IC 443 taken at 151 MHz with the Cambridge Low Frequency Synthesis Telescope and at 1419 MHz with the Cambridge Half-Mile Telescope, found significant variations in α across IC 443, with $\alpha < 0.46$ in the bright northeastern rim, and up to ~0.66 in the more diffuse southwestern region. He compares his results with those of Kundu & Velusamy (1986), who reported a spectral break in the emission from the bright northeastern rim ($\alpha = 0.1$ and 0.36 below and above 750 MHz, respectively), and a straight spectrum with $\alpha \sim 0.4$ in other regions of the remnant. A spectral break, however, is not evident in the integrated spectrum of IC 443, which can be fitted with a single power law with $\alpha = 0.36 \pm 0.02$ for frequencies above 20 MHz (Erickson & Mahoney 1985). Green suggests that the integrated spectrum can also be well fitted by a composite of different spectra arising in different emission features within the remnant: a broken spectrum associated with the northeastern rim, a straight spectrum in the southwestern diffuse emission, and flat spectra from line-of-sight thermal material. The observed spectral variations may be due to varying degrees of compression of magnetic field and an electron population with a broken energy spectrum (e.g., the Galactic CR pool), or a variation in prevalent emission enhancement mechanisms across the remnant (e.g., compression vs. Fermi acceleration).

It is interesting to note that IC 443, like G39.2−0.3, shows a faint plume of radio-emitting material extending from its shell (see, e.g., Green's image at 151 MHz; Plate 1, 1986). Green obtains an α of 0.8 ± 0.2 for the plume between 151 and 1419 MHz, suggesting the radio emission process is nonthermal. This plume is oriented along a set of optical filaments outside the main shell to the northeast which appear to be spectrally similar to other filaments found within the remnant (Fesen 1984). Fesen favors a model for these filaments involving a "breakout" of the SNR blastwave into a lower density region in the inhomogeneous medium surrounding IC 443.

6.4.3. *Cygnus Loop*

In the radio, the Cygnus Loop consists of a larger, limb-brightened shell to the north (toward the Galactic plane), with a lower surface brightness extension to the south. The conventional explanation for the morphology of the Cygnus Loop, as summarized by Green (1990), is that the remnant is expanding into a medium with a density gradient (decreasing away from the Galactic plane), and that the southern extension constitutes a "breakout" of the remnant into a lower density medium. As with IC 443, there is a detailed spatial correlation of optical filaments with fine-scale radio features (Dickel & Willis 1980). The Cygnus Loop, at ~10^4 years of age, appears globally to be in an adiabatic SNR evolutionary phase, with locally radiative shocks where the blast wave impinges on density enhancements in the surrounding medium (McKee & Cowie 1975).

The Cygnus Loop shows evidence for a possible break in its integrated radio spectrum at 1 GHz, with $\alpha = 0.38 \pm 0.04$ and 0.84 ± 0.4 below and above 1 GHz, respectively (De Noyer 1974, but see Green's reservations [1990]). The spatial spectral index variations observed in the Cygnus Loop are qualitatively similar to those observed in IC 443. In a comparison of data at 408 MHz (Green 1990) and 2695 MHz (Keen et al. 1973), Green measures a flatter spectral index associated with the bright northeastern rim ($\alpha = \sim 0.35$), while he finds indices in the south as steep as 0.5. This trend is confirmed qualitatively by previous spectral studies by Kundu & Becker (1972) and Sastry, Dwarakanath, & Shevgaonkar (1981). As with IC 443, Green suggests that varying compression of particles and fields may be responsible for the spectral variations, if the break in the integrated spectrum is real. Alternatively, the variations may be tied to the difference in shock speed between the north and the south, and hence the relative efficiency of different emission enhancement mechanisms.

6.4.4. *G127.1+0.5*

G127.1+0.5 is a fairly circular shell remnant, with a straight integrated radio spectrum of index 0.6 (Salter, Pauls, & Haslam 1978). No optical emission has been detected in associated with this remnant (Blair et al. 1980). Fürst, Reich, & Steube (1986) reported evidence for spectral variations in G127.1+0.5 based on observations at 1410 and 4850 MHz, and supported by data at 608.5 MHz (Pauls et al. 1982). The brightness distribution around the shell at 4850 MHz is highly asymmetric, being a factor of 2 brighter toward the Galactic north (away from the Galactic plane). The asymmetry decreases at 1410, and at 608.5 MHz the distribution is fairly even. Fürst et al. estimate spectral indices of $\alpha \sim 0.35$ and 0.55 for the north and south, respectively.

The magnetic field orientation in G127.1+0.5, inferred from measurements of linear polarization angle (Fürst et al. 1984), is consistent with blastwave compression of an ambient magnetic field. They show that the van der Laan compression model (van der Laan 1962), in conjunction with the Sedov equations, is consistent with their radio data, although they offer no explanation for the apparent spectral variations. Their calculations yield an age for the remnant of 50,000–120,000 yr.

6.4.5. *S 147*

S 147 exhibits a circular shell radio morphology, with brightness enhancements toward the (Galactic) north and east. It is a relatively old shell, with an estimated age of 10^5 yr, and is presumably in a radiative evolutionary phase (Sofue, Fürst, & Hirth 1980; Kundu et al. 1980). S 147 exhibits a remarkably

detailed spatial correlation between radio emission features and optical filaments. Like the Cygnus Loop, S 147 also shows evidence for a break at 1 GHz in its integrated spectrum (Kundu et al. 1980; Angerhofer & Kundu 1981).

Fürst & Reich (1986) determined the spectral index distribution in S 147 from Effelsberg observations at 1425 and 2695 MHz. They found that the radio-bright north and eastern parts of the shell (corresponding to regions of bright optical filamentation) were flatter than the more diffuse southwestern part of the remnant, with typical spectral indices of ~ 0.5 and 0.9, respectively. When the small scale structure is separated from the diffuse emission through spatial filtering, similar results are obtained: the small-scale emission has $\alpha = 0.4 \pm 0.15$ between 1425 and 2695 MHz, while the diffuse component has $\alpha = 0.9 \pm 0.15$ (Fürst & Reich 1988). Between 1425 and 4750 MHz, spectral indices of $\alpha \sim 0.5$ and 1.0 are obtained for the small- and large-scale structure, respectively. The authors explore explanations which involve compression of a bent spectrum electron population, as is presumably reflected in the integrated spectrum.

6.4.6. *Puppis A*

Puppis A, at an estimated age of 3700 yr (Winkler et al. 1988), appears to still be in a nonradiative phase, based on the lack of correlation between radio and optical features (Dubner et al. 1991). Observations at X-ray, optical, infrared, and radio wavelengths suggest that Puppis A is interacting with a molecular cloud to its east, which is observed in the IR (Arendt et al. 1990), and in H I and CO (Dubner & Arnal 1988). The interaction appears to be decelerating the eastern edge of the remnant, leading to the observed compacted and dented radio morphology of the shell along this edge (Dubner et al. 1991). Arendt et al. (1990) also report evidence for a second, less dense cloud, perhaps impinging on the remnant at an enhancement in the radio and IR shell to the south. Dubner et al. (1991) undertook a spectral study of Puppis A to determine whether deceleration was having an effect on the spectral index distribution within the remnant.

Based on VLA observations at 327 and 1515 MHz, Dubner et al. derived an integrated spectral index of 0.53 for Puppis A, which is consistent with an earlier multifrequency estimate by Milne (1971). The distribution of spectral indices was estimated by integrating flux densities in specified regions within the remnant. They found a steeper index of 0.67 associated with the eastern side of the remnant, with other regions, including the southern brightening, being close to the integrated α. The authors suggest the steepening may be associated with an enhanced deceleration of ejecta in this part of the shell due to the presence of the eastern cloud.

6.4.7. *Cassiopeia A*

Cassiopeia A, a 300 year old shell remnant, has a radio morphology consisting of a bright, clumpy shell sitting atop a faint, diffuse plateau. The remnant also contains a number of high emissivity compact structures, such as the "bow shocks" identified by Braun, Gull, & Perley (1987). Cas A is thought to be currently undergoing a transition from the free expansion stage of SNR evolution to the Sedov stage. According to models by Gull (1973), this transition is accompanied by a rapid amplification of magnetic field strength, thus betatron particle acceleration may be active in the remnant at this time. In addition, particles may also be accelerated in turbulence set up by the dynamical instabilities which accompany this phase change. First-order acceleration processes at shocks must also be considered.

Anderson et al. (1991) identified spectral index variations in Cas A between $\alpha = 0.6$ and 0.9, derived from VLA observations at 1.4 and 5.0 GHz. The steeper regions in the remnant tend to be associated with bright, compact features, while the flatter indices were found almost exclusively in the large-scale radio ring. Most of Braun, Gull, & Perley's bow shock structures were found to have spectral indices steeper than the remnant mean. These features are presumably young, as indicated by their compact structure and rapid evolution in brightness and morphology. It was suggested that the difference in spectral indices between the bow shocks and the ring, under first-order Fermi considerations, may be due to different local sound speeds as indicated by fitted X-ray temperatures (Jasen et al. 1988). However, it has been shown (Anderson et al. 1991) that the steep spectral indices and high emissivities associated with the bow shocks are not concomitantly consistent with first-order acceleration, thus this explanation is likely oversimplified.

6.5. *Synopsis*

To facilitate a comparison between the spectral variations observed in the SNRs discussed above, we group the remnants into two categories, based loosely on estimated age: the "older" remnants (greater than several thousand years: IC 443, the Cygnus Loop, G127.1+0.5 and S 147), and the "younger" remnants (less than a few thousand years: Puppis A, Cas A and G41.1−0.3). Note that our age designations of "young" and "old" are somewhat nonstandard and should be considered only in a relative sense. The two remnants with centrally enhanced radio emission (G33.6+0.1 and G39.2−0.3) are considered separately.

In the "older" shell remnants showing spatial spectral index variations, the high emissivity parts of the shell are flatter than the other parts of the remnant, including the diffuse emission. These high emissivity regions are typically attributed to an interaction between the shell and a density enhancement in the surrounding medium.There is generally a good correlation between the small-scale radio and optical features in these regions, indicating that the shocks there are probably radiative and thus highly compressive. If the spectral breaks observed in IC 443, the Cygnus Loop and S 147 are real, the spectral variations observed in these remnants can be consistently interpreted as variations in magnetic field strength. G127.1+0.5, however, shows no breaks in its integrated spectrum, although perhaps a composite spectrum could be constructed such as was suggested by Green (1986) for IC 443.

Even if these spectral bends are proven to be merely instrumental artifacts, we are still left with the observation that regions of older remnants in this sample which appear to be confined are consistently flatter than are more freely expanding parts of the remnants. Local electron energy spectra must therefore be directly tied to conditions instigated in SNR-cloud interactions.

The situation with the "younger" remnants is less clear. In Puppis A and Cas A, the highest emissivity regions tend to be associated with steeper indices. In G41.1−0.3, steep spectra are found near, but not spatially coincident with, the brightest part of the remnant. It is difficult to obtain both high-emissivity and steep spectral indices concurrently from first-order acceleration models (see discussion in Anderson et al. 1991 concerning Cas A). Other mechanisms, such as acceler-

ation in cosmic-ray-mediated shocks and turbulent acceleration, should be tested for applicability in these cases; however, at present, numerical simulations of SNR evolution with these forms of acceleration do not include studies of the evolving particle spectra, due to prohibitive computational expense. On the other hand, it may be that in these remnants, radio luminosity and spectral index are being regulated by different mechanisms. This must certainly be the case for G41.1−0.3, where a large region of steep spectral index spans both bright and faint filamentary structures. Dickel et al. (1989), for example, have suggested that brightness inhomogeneities in young shell remnants are due to localized amplification of magnetic fields in the turbulence stimulated by the onset of dynamical instabilities where the ejecta encounter clouds in the surrounding medium, while the electron energy spectra are determined predominantly by first-order acceleration at shocks. Hybrid scenarios of this type may be needed to explain the spectral and brightness variations in these less-evolved remnants.

The two remnants with enhanced central emission, G39.2−0.3 and G33.6+0.1 are special cases. In both SNRs, the flattest spectra are associated with emission interior to the shell (although in G39.2−0.3 the region of flattening is not precisely coincident with the central emission enhancement). More exotic explanations may need to be invoked for these remnants, such as an acceleration of particles by unseen internal pulsars. We are also left with the puzzle of the flat spectrum plume in G39.2−0.3. High-sensitivity polarimetric radio observations are needed to determine whether this emission is thermal or nonthermal in origin.

6.6. *Intra- vs. Inter-Remnant Spectral Variations*

It appears that there are a number of environmental and evolutionary factors that may determine the spatial distribution of synchrotron spectral index within a given shell remnant. Do these same factors operate on a larger scale as well to determine the variations in *integrated* spectral index ($\alpha_{\rm integ}$) observed among different shell remnants? It should be noted that the spread in spectral indices found within individual remnants listed in §§ 6.2–6.4 ($\Delta\alpha$ on the order of ± 0.1) is much smaller than the range in integrated index associated with the shell class as a whole ($\Delta\alpha_{\rm integ} \sim \pm 0.3$). Therefore, if the spread in $\alpha_{\rm integ}$ is a predominantly environmental effect, the most important determining factors must be varying appreciably over scales much larger than a remnant size (Green 1988). Green, however, has noted a correlation between $\alpha_{\rm integ}$ and remnant diameter for those shells with well-determined distances (flattening with increasing size), suggesting the inter-remnant variations may be tied to evolutionary stage. This might be expected if the trends listed in § 6.1 hold for all shell remnants. If bright parts of older remnants are flat, while the flux/spectrum relationship is mixed for younger remnants, then we would expect a size-$\alpha_{\rm integ}$ relationship, as suggested by Green.

Statistical studies of integrated spectral index are a difficult chore, given the current state of SNR compendia. Green (1991) warns that critical biases exist in his catalog, based in the fact that the major SNR surveys in different parts of the Galactic plane have been conducted with different telescopes and with different sensitivity limits and resolutions. These biases are also expressed in the integrated spectral indices quoted in this catalog. In addition, the method of baseline subtraction, the absolute flux scale, and the number and distribution of frequencies used in the index determination can greatly affect the outcome. Loss of sensitivity at large spatial scales is an issue in interferometric total flux density measurements. All of these effects typically vary from experiment to experiment, and have not been corrected for in the most complete SNR catalogs.

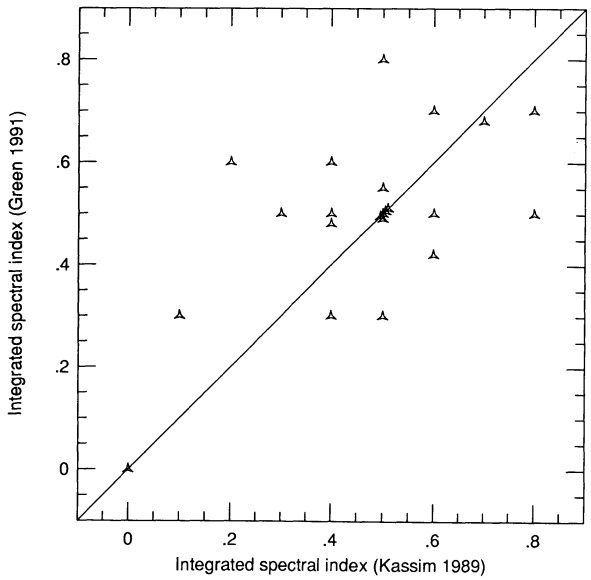

FIG. 7.—A comparison of integrated spectral indices derived by Kassim (1989) for 26 Galactic SNRs and indices quoted in Green's catalog (1991).

Figure 7 demonstrates the scatter that is introduced into integrated spectral index estimates by using different measurement techniques. Green's catalog (1991) is the most extensive listing of SNRs and their spectral indices to date. The spectral indices quoted in this catalog are derived from the literature and represent a variety of observational techniques. In Figure 7, Green's spectral indices (those which he deemed reliable in this catalog) are plotted vs. spectral indices derived by Kassim (1989). Kassim has taken all flux density measurements from the literature for 32 Galactic SNRs, supplemented with new low-frequency measurements, edited out those data which he considered less reliable, and brought all points to a common flux scale. His spectral fits include a possible low-frequency turnover due to absorption. The scatter in Figure 7 is quite significant. The most discrepant indices ($\Delta\alpha \geq 0.3$) were derived from fits to a small number of points (≤ 6, from Kassim's listing). A complete catalog of integrated spectral indices, determined in a self-consistent manner from data bases well-sampled in frequency, is needed before accurate statistical studies can be conducted.

7. CONCLUSIONS

1. We have found spatial variations in radio spectral index on the order of $\Delta\alpha \sim 0.2$ in the Galactic shell SNRs G39.2−0.3 and G41.1−0.3. Given the handful of shells that are now known to exhibit spectral variations, the canonical view that all shell remnants have spatially uniform spectra must be discarded.

2. The spectral variations in G39.2−0.3 and G41.1−0.3 do not coincide with features in total intensity, that is, regions of constant spectral index may span a large range in synchrotron

brightness. Thus these variations must be tied to aspects of the hydrodynamic flow which is not necessarily important to synchrotron emissivity.

3. In comparing nine shell remnants with reported spectral variations, we find that in the "older" remnants (>several thousand years), bright regions are spectrally flatter than more diffuse regions. This correlation may be due, in some cases, to varying degrees of compression of an electron population with an intrinsically bent energy spectrum (e.g., Galactic cosmic-ray electrons). Alternatively, if the intrinsic electron energy spectra in these remnants are straight, it is clear that collisions between the SNR blastwave and external clouds serve to flatten local spectra. This may be related to the increase in Mach number as the blastwave enters the denser cloud environment.

4. In the "younger" remnants included in our comparison (those with ages less than a few thousand years), bright regions are found to be both flat *and* steep. Thus, as stated above, spectral variations in these SNRs may be regulated by different mechanisms than are the brightness variations.

5. It is not clear if or how the agents responsible for the spatial spectral variations in individual remnants are related to those which determine the large spread in integrated spectral index observed among shell SNRs as a class. To tackle this question, we will need a comprehensive list of consistently measured integrated spectral indices for reliable statistical analyses.

6. Given the complicated relationships we have found to exist between spectral indices and structures in total synchrotron intensity, a clear interpretation of these spectral variations must await a more thorough understanding of the hydrodynamics of SNR evolution in a clumpy medium and the efficiencies of electron injection and acceleration.

This work was supported, in part, by the NSF through grants AST-872085 and AST-9100486. We wish to thank T. W. Jones and S. P. Reynolds for very helpful discussions and comments. Thanks also to D. H. Porter and B. K. Edgar for their help in printing out images presented here.

REFERENCES

Anderson, M., Rudnick, L., Leppik, P., Perley, R., & Braun, R. 1991, ApJ, 373, 146
Angerhofer, P. E., & Kundu, M. R. 1981, AJ, 86, 1003
Arendt, R. G., Dwek, E., Petre, R., Dickel, J. R., Roger, R. S., Milne, D. K., & Kesteven, M. J. 1990, ApJ, 350, 266
Baars, J. W. M., Genzel, R., Pauliny-Toth, I. I. K., & Witzel, A. 1977, A&A, 61, 99
Becker, R. H., & Helfand, D. J. 1987, AJ, 94, 1629
Becker, R. H., Markert, T., & Donahue, M. 1985, ApJ, 296, 461
Bell, A. R. 1978, MNRAS, 182, 147
Blair, W. P., Kirshner, R. P., Gull, T. R., Sawyer, D. L., & Parker, R. A. R. 1980, ApJ, 242, 592
Braun, R., Gull, S. F., & Perley, R. A. 1987, Nature, 327, 395
Bridle, A. H. 1967, MNRAS, 136, 219
Caswell, J. L. 1977, Proc. Astron. Soc. Australia, 3, 130
Caswell, J. L., Haynes, R. F., Milne, D. K., & Wellington, K. J. 1982, MNRAS, 200, 1143
Caswell, J. L., & Lerche, I. 1979, MNRAS, 187, 201
Cersosimo, J. C., & Magnani, L. 1990, A&A, 239, 287
Clark, D. H., & Caswell, J. L. 1976, MNRAS, 174, 267
Cornwell, T. J., & Evans, K. F. 1985, A&A, 143, 77
De Noyer, L. K. 1974, AJ, 79, 1253
———. 1977, ApJ, 212, 416
Dickel, J. R., Eilek, J. A., Jones, E. M., & Reynolds, S. P. 1989, ApJS, 70, 497
Dickel, J. R., & Willis, A. G. 1980, A&A, 85, 55
Dubner, G. M., & Arnal, E. M. 1988, A&AS, 75, 363
Dubner, G. M., Braun, R., Winkler, P. F., & Goss, W. M. 1991, AJ, 101, 1466
Duin, R. M., & van der Laan, H. 1975, A&A, 40, 111
Eilek, J. A., & Henriksen, R. N. 1984, ApJ, 277, 280
Ellison, D. C., & Reynolds, S. P. 1991, ApJ, 382, 242
Erickson, W. C., & Mahoney, M. J. 1985, ApJ, 290, 596
Fesen, R. A. 1984, ApJ, 281, 658
Fürst, E., & Reich, W. 1986, A&A, 163, 185
———. 1988, in Supernova Shells and Their Birth Events, ed. W. Kundt (Berlin: Springer), 33
Fürst, E., Reich, W., & Steube, R. 1984, A&A, 133, 11
Green, D. A. 1986, MNRAS, 221, 473
———. 1988a, in Genesis and Propagation of Cosmic Rays, ed. M. M. Shapiro & J. P. Wefel (Dordrecht: Reidel), 205
———. 1988b, Ap&SS, 148, 3
———. 1990, AJ, 100, 1927
Green, D. A. 1991, PASP, 103, 209
Green, D. A., & Dewdney, P. E. 1992, MNRAS, 254, 686
Gull, S. F. 1973, MNRAS, 161, 47
Högbom, J. A. 1974, A&AS, 15, 417
Jansen, F., Smith, A., Bleeker, J. A. M., de Korte, P. A. J., Peacock, A., & White, N. E. 1988, ApJ, 331, 949
Kang, H., & Jones, T. W. 1990, ApJ, 353, 149
———. 1991, MNRAS, 249, 439
Kassim, N. E. 1989, ApJ, 347, 915
Keen, N. J., Wilson, W. E., Haslam, C. G. T., Graham, D. A., & Thomason, P. 1973, A&A, 28, 197
Kundu, M. R., Angerhofer, P. E., Fürst, E., & Hirth, W. 1980, A&A, 92, 225
Kundu, M. R., & Becker, R. H. 1972, AJ, 77, 459
Kundu, M. R., & Velusamy, T. 1968, MNRAS, 140, 173
McKee, C. F., & Cowie, L. L. 1975, ApJ, 195, 715
Milne, D. K. 1971, Australian J. Phys., 24, 429
Mufson, S. L., McCollough, M. L., Dickel, J. R., Petre, R., White, R., & Chevalier, R. 1986, AJ, 92, 1349
Napier, P. J., Thompson, A. R., & Ekers, R. D. 1983, Proc. IEEE, 71, 1295
Narayan, R., & Nityananda, R. 1986, ARA&A, 24, 127
Parkes, G. E., Charles, P. A., Culhane, J. L., & Ives, J. C. 1977, MNRAS, 179, 55
Patnaik, A. R., Hunt, G. C., Salter, C. J., Shaver, P. A., & Velusamy, T. 1990, A&A, 232, 467
Pauls, Y., van Gorkom, J. H., Goss, W. M., Shaver, P. A., Dickey, J. M., & Kulkarni, S. 1982, A&A, 112, 120
Roger, R. S., Milne, D. K., Kesteven, R. F., Haynes, R. F., & Wellington, K. J. 1985, Nature, 316, 44
Salter, C. J., Pauls, T., & Haslam, C. G. T. 1978, A&A, 66, 77
Sastry, Ch. V., Dwarakanath, K. S., & Shevgaonkar, R. K. 1981, J. Astrophys. Astron., 2, 339
Scheuer, P. A. G. 1984, Adv. Space Res., 4, 337
Schlickeiser, R., & Fürst, E. 1989, A&A, 219, 192
Shaver, P. A. 1982, A&A, 105, 306
Sofue, Y., Fürst, E., & Hirth, W. 1980, PASJ, 31, 1
van der Laan, H. 1962, MNRAS, 124, 125
Velusamy, T., Becker, R. H., & Seward, F. D. 1991, AJ, 102, 676
Whiteoak, J. B. Z. 1990, Nature, 347, 157
Winkler, P. F., Turtle, J. H., Kirshner, R. P., & Irwin, M. J. 1988, in Supernova Remnants and the Interstellar Medium, ed. R. S. Roger & T. Landecker (Cambridge: Cambridge Univ. Press), 65